



# Influence of Liquid Nitrogen Cooling State on Mechanical Properties and Fracture Characteristics of Coal

Peng Hou<sup>2</sup> · Shanjie Su<sup>1,3</sup> · Feng Gao<sup>3</sup> · Xin Liang<sup>4</sup> · Shengcheng Wang<sup>1</sup> · Yanan Gao<sup>3</sup> · Chengzheng Cai<sup>3</sup>

Received: 31 July 2021 / Accepted: 9 March 2022 / Published online: 23 March 2022  
© The Author(s), under exclusive licence to Springer-Verlag GmbH Austria, part of Springer Nature 2022

## Abstract

To determine the role of LN<sub>2</sub>-cooling in the fracturing process of the coal, the LN<sub>2</sub>-cooling process of the coal samples is divided into three states: initial state, frozen state, and freeze–thaw state. Changes in the mechanical properties and fracture behaviors of the coal samples under three states are systematically evaluated by a series of laboratory experiments. The thermal cracking behavior of the coal during LN<sub>2</sub> freeze–thaw is revealed through a crack phase-field model. The results indicate that the compressive strength, elastic modulus, and fracture toughness of the frozen coal significantly increase, while they decrease for the freeze–thaw coal. The tensile strength of the coal under the freeze and freeze–thaw states has an obvious reduction, where a greater decrease for the freeze–thaw coal is induced. The fracture propagation process and induced fracture morphology of the coal under both the freeze and freeze–thaw states become complex, in which a greater change for the freeze–thaw coal is presented. The micro-fracture in the coal during LN<sub>2</sub>-cooling mainly comes from the temperature gradient and mismatch of thermal stress between adjacent mineral particles. Both fracture growth rate and fracture area in the LN<sub>2</sub> thaw process are larger than that in the LN<sub>2</sub> freeze process. The variations in the fracturing behaviors of the coal with different LN<sub>2</sub> treatment states in the mechanical experiments are well explained by the numerical simulation results.

## Highlights

- The mechanical properties of the coal with different LN<sub>2</sub> cooling states are studied systematically through laboratory experiments.
- Effects of the LN<sub>2</sub> cooling state on the crack propagation and fracture morphology of the coal in the mechanical tests are analyzed.
- The micro-crack evolution process of the coal during the LN<sub>2</sub> freeze–thaw is revealed through a crack phase-field model.
- Both the crack propagation rate and induced crack area inside the coal during the LN<sub>2</sub> thaw process are greater than that during the LN<sub>2</sub> freeze process.

**Keywords** Coal · Liquid nitrogen fracturing · Mechanical properties · Fracture characteristics · Crack phase field

---

✉ Shanjie Su  
sushanjie@cumt.edu.cn; sushanjie@xzit.edu.cn

<sup>1</sup> School of Civil Engineering, Xuzhou University of Technology, Xuzhou 221018, Jiangsu, China

<sup>2</sup> IPPH, Purdue University, West Lafayette, IN 47907, USA

<sup>3</sup> State Key Laboratory for Geomechanics and Deep Underground Engineering, China University of Mining and Technology, Xuzhou 221116, Jiangsu, China

<sup>4</sup> School of Civil Engineering and Architecture, Xi'an University of Technology, Xi'an 710048, Shaanxi, China

## Abbreviations

CBM	Coalbed methane
QSGS	Quartet structure generation set
RA	Rise time/amplitude

## List of symbols

$\sigma_t$	Tensile strength
$K_I$	Mode I fracture toughness
$P_{\max}$	Maximum loading
$D$	Diameter of the disk
$Y_I$	Geometry factor
$t$	Time
$T$	Temperature
$\bar{T}$	Specified boundary temperature
$\bar{Q}$	Specified boundary heat source
$h$	Convective parameter of heat exchange
$Q$	Heat source
$c_p$	Heat capacity
$\rho$	Density of the coal
$k$	Heat conductivity
$\mathbf{n}^T$	Normal unit vector
$\boldsymbol{\sigma}$	Stress tensor
$\mathbf{F}_V$	Volumetric force tensor
$\mathbf{D}$	Elasticity modulus tensor
$\mathbf{u}$	Displacement tensor
SEM	Scanning electron microscope
AE	Acoustic emission
ISRM	International Society for Rock Mechanics
AF	AE counts/duration
$\boldsymbol{\epsilon}^e$	Elastic strain
$\boldsymbol{\epsilon}^{th}$	Thermal strain
$T_0$	Reference temperature
$\boldsymbol{\alpha}_T$	Thermal expansion tensor.
$\phi$	Phase field
$d(\phi)$	Damage function
$l_{\text{int}}$	Internal length scale
$H_d$	State variable function
$G_c$	Critical energy release rate
$G_{c0}$	Strain energy threshold
$W_{s0}^+$	Tensile part of the undamaged elastic strain energy density
$\boldsymbol{\epsilon}_{\text{el}}^+$	Tensile part of the elastic strain tensor
$\boldsymbol{\epsilon}_{\text{el},\text{pi}}$	Principal value of the elastic strain tensor
$\mathbf{n}_i$	Direction vector
$\mathbf{C}$	4th order elasticity tensor
$k_0$	Initial thermal conductivity
$g(\phi)$	Stiffness weakening function
$\mathbf{D}_0$	Initial elasticity modulus tensor
$\nu$	Poisson's ratio
$E$	Elastic modulus

## 1 Introduction

Since conventional energy resource is increasingly exhausted, coalbed methane (CBM), as an unconventional resource with enormous reserves, has attracted more attention around the world. CBM extraction can not only reduce gas outburst risk greatly but improve greenhouse gas emission positively (Dong et al. 2017; Liu et al. 2018; Pan et al. 2014). However, CBM adsorbed in micro-pore and micro-crack of coal is difficult to extract economically due to the low permeability feature of coal (Li et al. 2017; Liu et al. 2009), thus stimulation technologies of CBM reservoir are urgently needed. Currently, hydraulic fracturing (Liang et al. 2021a, b), as a relatively mature fracturing method, is widely used in CBM extraction and effectively increases CBM extraction efficiency. Nevertheless, during hydraulic fracturing, the invasion of the water phase causes water lock and water-sensitivity damages to the reservoir (Anderson et al. 2010). Moreover, lots of water resources are consumed and the proppant carried in water-based fracturing fluid enters the aquifer to pollute the groundwater (Pelak and Sharma 2014). Thus, many investigations on waterless fracturing techniques have developed rapidly, such as the high energy gas fracturing technology (Liew et al. 2020), the CO<sub>2</sub>/N<sub>2</sub> fracturing technology (Hou et al. 2018; Middleton et al. 2014), the cryogenic fracturing technology (Cha et al. 2014; Su et al. 2020, 2022), and so on. Liquid nitrogen (LN<sub>2</sub>) with ultra-low cryogenic temperature of -196 °C can promote cracks appearing and extending in rocks due to the huge thermal stress (Wu et al. 2019; Hou et al. 2021c, 2022), and it has been proved feasible to use thermal treatment technology to improve CBM production (McDaniel et al. 1998). In summary, LN<sub>2</sub> fracturing offers many advantages in enhancing the stimulation effect, saving water resources, and protecting reservoirs.

In the LN<sub>2</sub> fracturing of coal, the cryogenic fracturing effect of LN<sub>2</sub> plays a key role, which has been studied by many scholars. Previous studies can be mainly divided into three aspects: structural alteration, mechanic property change, and heat transfer characteristics of coal before and after LN<sub>2</sub> cooling. The heat transfer law in coal during LN<sub>2</sub> fracturing has been reported from the perspective of numerical simulation and experiment, which is helpful to understand the damage mechanism of coal during LN<sub>2</sub>-cooling (Li et al. 2020a; Wu et al. 2018). Through the LN<sub>2</sub> soaking tests of the coal, the temperature changes of coal can be divided into three stages: accelerated cooling, decelerated cooling, and low-temperature maintenance (Liu et al. 2021). Based on the isotropy assumption and thermo-mechanical

coupling model, Du et al. (2020b) found that the surface and central parts of the coal sample are subjected to tensile stress and compressive stress, respectively. The maximum thermal stress induced by LN<sub>2</sub> cryotherapy occurred at the surface of the specimens. The permeability of coal is closely related to the degree of pore-fracture development (Hou et al. 2021a, b). Ren et al. (2013) performed the ultrasonic wave velocity tests on coal and found that both the wave velocity and amplitude of coal decrease after LN<sub>2</sub>-cooling. Coetzee et al. (2014), Zhai et al. (2016), and Qin et al. (2021, 2022) discovered that LN<sub>2</sub>-cooling treatment can greatly increase the number and connectivity of pores inside coal. Chu and Zhang (2019) and Chu et al. (2020) compared the changes in the pore/fracture structure inside coal before and after LN<sub>2</sub> thermal shock load. Yan et al. (2020a, b) explored the evolution characteristics of fractures inside coal after LN<sub>2</sub>-cooling using micro-X-ray computed tomography, including the porosity, fracture volume, fracture thickness, and fracture connectivity. Therefore, the permeability of coal subjected to LN<sub>2</sub>-cooling is improved due to the increase of pore connectivity and the generation of microcracks. The mechanical properties of coal will be deteriorated due to changes in its internal structure after LN<sub>2</sub>-cooling treatment. The elastic modulus, compressive strength, and tensile strength of coal subjected to LN<sub>2</sub> cryotherapy decrease significantly (Cai et al. 2016, 2018; Jin et al. 2019; Li et al. 2020b), and the fracture propagation becomes more active during the mechanical experiments.

Although the above studies have provided some noteworthy information about the LN<sub>2</sub> fracturing of coal, the coal stimulation using such a method still needs a better understanding to be encouraging practically. Previous laboratory experiments are mainly focused on the changes in physical and mechanical characteristics of coal before and after LN<sub>2</sub> cooling. However, few investigations have paid attention to the influence of the LN<sub>2</sub>-cooling state (namely, temperature change) on the physical and mechanical properties of coal. During LN<sub>2</sub> fracturing, coal is actually subjected to two thermal shock loadings: freeze process and thaw process (Liu et al. 2020b, 2021). Cai et al. (2018) found that the P-wave velocity and tensile strength of the frozen coal decreased by 14.46 and 17.39%, respectively, 14.46 and 17.39% for the freeze–thaw coal, respectively. The results indicate that the LN<sub>2</sub>-cooling state plays an important factor in LN<sub>2</sub> fracturing. Currently, there also has been no systematic study on the effects of LN<sub>2</sub>-cooling on different mechanical parameters of coal. For example, fracture toughness, as one parameter of rock mechanical properties, reflects the resistance of the rock to crack growth and plays a key role in the design of fracturing technology. However, it is rarely reported. Meanwhile, the damage mechanism of coal subjected to LN<sub>2</sub>-cooling also needs to be further studied. In the previous isotropic thermal–mechanical coupling model, only

the temperature gradient effect is studied. However, the mismatch of thermal stress between adjacent mineral particles has also a significant influence on the rock cracking due to the anisotropic characteristics of the rock (Wu et al. 2019). Therefore, this study aims to systematically investigate the mechanical properties and fracture behaviors of coal subjected to different LN<sub>2</sub> cooling states, and quantitatively reveal the thermal damage evolution process of coal during LN<sub>2</sub> thermal shock.

In this study, the LN<sub>2</sub>-cooling process of the coal samples is divided into three special states: initial state, frozen state, and freeze–thaw state. Then, systematic mechanical experiments are carried out on the coal under these three states, including the uniaxial compression experiment, Brazilian splitting experiment, and three-point bending experiment. The crack propagation and failure characteristics of the coal samples under the three states are compared through a series of auxiliary experiments. Finally, the micro-fracture propagation mechanism of the coal during LN<sub>2</sub> thermal shock is quantitatively revealed based on a thermo-mechanical coupling phase-field model, the change in the fracturing behavior of the coal under three states is explained. The

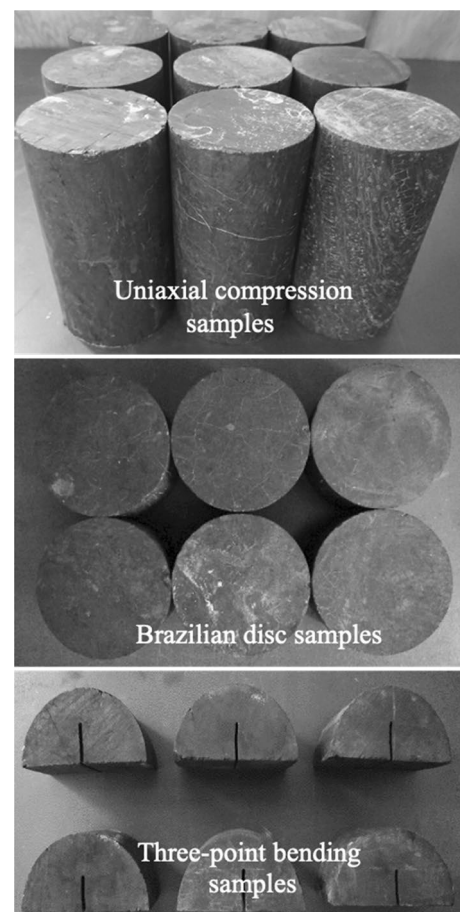


Fig. 1 Coal samples

results are expected to have a strong guiding role for the development of LN<sub>2</sub> fracturing in the low-permeability coal.

## 2 Material Preparation and Methods

### 2.1 Sample Preparation

The experimental coal samples are all taken from the Yulin mining area of Shanxi Province. After the coal is mined, it is transported to the laboratory under sealed conditions, and then the equipment is used to drill, cut, grind, and slit the raw coal. After the processing, the coal samples are shown in Fig. 1. The moisture content of the coal is 5.47%. In addition, the coal samples are taken from the same raw coal to reduce the influence of the coal heterogeneity on the experimental results. The standard cylinder sample with a height of 100 mm and a diameter of 50 mm is used in the uniaxial compression experiment. The disc sample with a thickness of 25 mm and a diameter of 50 mm is employed in the Brazilian splitting experiment. The semi-disc specimen with a thickness of 25 mm and a diameter of 50 mm is used in the three-point bending experiment, where the width and length of the artificial slit are 1 and 12.5 mm, respectively. The surface flatness, width, and verticality of prefabricated cracks of the coal samples are within the tolerance range recommended by the International Society for Rock Mechanics (ISRM). The processed coal samples used in the experiment are all dried and then sealed with plastic wrap for later use.

### 2.2 Experimental Methods

In the LN<sub>2</sub> cooling tests, three LN<sub>2</sub>-cooling states are designed (Fig. 2), that is, untreated state, LN<sub>2</sub> freeze state, and LN<sub>2</sub> freeze–thaw state. The untreated group is the control group. The coal samples on the frozen group are

immersed in LN<sub>2</sub> for 1 h until completely frozen. To reduce deviations caused by the exposure of the frozen coal samples to room temperature, the structural and mechanical tests are carried out immediately when the frozen coal samples are taken out of LN<sub>2</sub>. Based on the results of a continuous ultrasonic test during the thawing process of the coal samples, this short exposure process has a slight effect on the surface structure of the coal sample, resulting in a 5.96% reduction in the P-wave velocity in 10 min. However, we believe that this is not enough to affect the overall structure of the sample. In the freeze–thaw group, the coal samples are frozen in the LN<sub>2</sub> container for 1 h, then put into a sealed bag and warmed to room temperature (about 4 h). Therefore, there are two thermal shock processes during the freeze–thaw. In addition, the mass and P-wave velocity of the samples in the freeze–thaw group are measured by the electronic scale and ultrasonic detector, respectively; their values under three states are taken from the same specimen. The changes in the microstructure of the coal before and after LN<sub>2</sub>-cooling treatment are observed by the scanning electron microscope (SEM). Three samples were tested for each case.

In the uniaxial compression experiment, the TAWD-2000 electro-hydraulic servo rock mechanical properties testing system is employed. The axial force control is used, and the loading rate is 100 N/s. The loading stops when the sample is destroyed. At the same time, the acoustic emission (AE) probe of the AE system PCI-2 is installed on the surface of the sample to monitor the crack propagation in real-time. To ensure the accuracy of the results, the Brazilian split and three-point bending experiments are performed using the CSS-88020 universal test machine, because the tensile strength and fracture toughness of the coal samples are relatively small. In both of these experiments, the axial displacement control is adopted, and the control speed is 0.005 mm/s. The distance between the

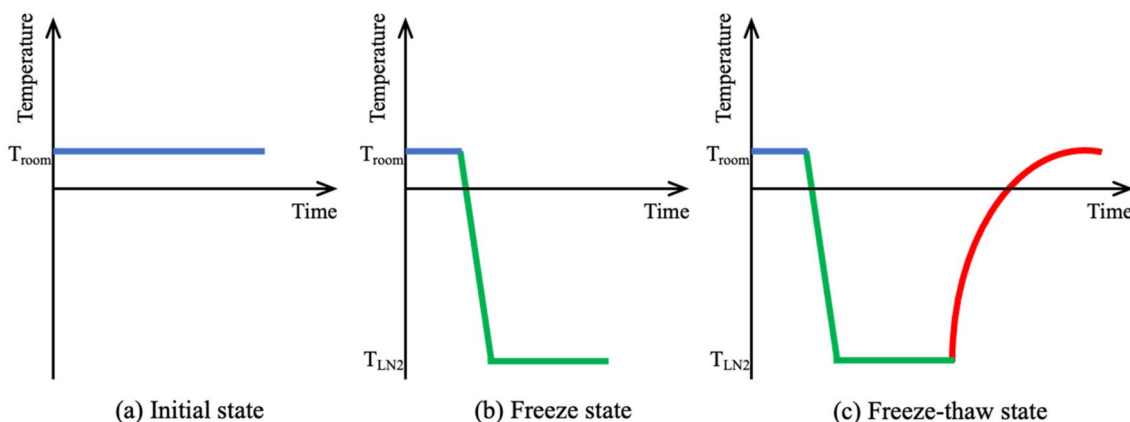


Fig. 2 Sketch map of three LN<sub>2</sub>-cooling states

next two supports is 12.5 mm in the three-point bending test. The load, displacement, and other information in the loading process are observed and recorded in real-time. The tensile strength (Garcia et al. 2017) and fracture toughness (Lim et al. 1993) of the coal samples are calculated by Eqs. (1) and (2), respectively:

$$\sigma_t = \frac{2P_{\max}}{\pi DB}, \tag{1}$$

$$K_I = \frac{P_{\max}}{DB} Y_I \sqrt{\pi a}, \tag{2}$$

where  $\sigma_t$  is the tensile strength,  $K_I$  is the mode I fracture toughness,  $P_{\max}$  is the maximum loading,  $D$  is the diameter of the disk;  $B$  is the disk thickness,  $Y_I$  is the geometry factor that depends on the normalized crack length and normalized

span ratio. Based on the study of Lim et al. (1993), the value of  $Y_I$  is 3.61 in this study.

After the completion of the mechanical test, the broken rock samples are sealed in a bag and marked well for subsequent analysis. As to the failure specimen after the uniaxial compression test, the fragment sizes of the coal are graded through the particle sizing screen, and five grades are used (that is: < 2 mm, 2–5 mm, 5–10 mm, 10–15 mm, > 15 mm). The total crack length of the damaged specimen after the Brazilian splitting experiment is calculated based on the binarization image of the failure pattern. After the three-point bending experiment, the main fracture surface of the sample is scanned by the 3D profilometer VR-5000, and then the fractal dimension of the 3-D fracture surface is calculated.

### 3 Experimental Results

#### 3.1 Structure Damage

Figure 3 shows changes in the surface structure of the coal sample under different states. Lots of thermal cracks on the coal sample surface after freezing are observed, indicating that the low temperature can promote the initiation and propagation of cracks during the freezing process. After the LN<sub>2</sub> thaw, the crack width on the specimen surface significantly reduces, and some weakly cemented matrix particles fall off. There may be two reasons for the crack closure during the thawing process. The first is that the low temperature in the frozen state will lead to the shrinkage of the coal matrix. After thawing, the coal matrix will resume deformation, leading to the crack closure. The second is the melting of the ice that supports the crack opening of the coal during the

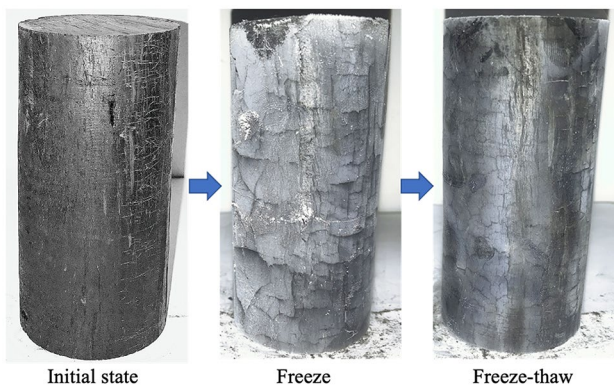


Fig. 3 Changes in the surface structure of the coal sample under different states

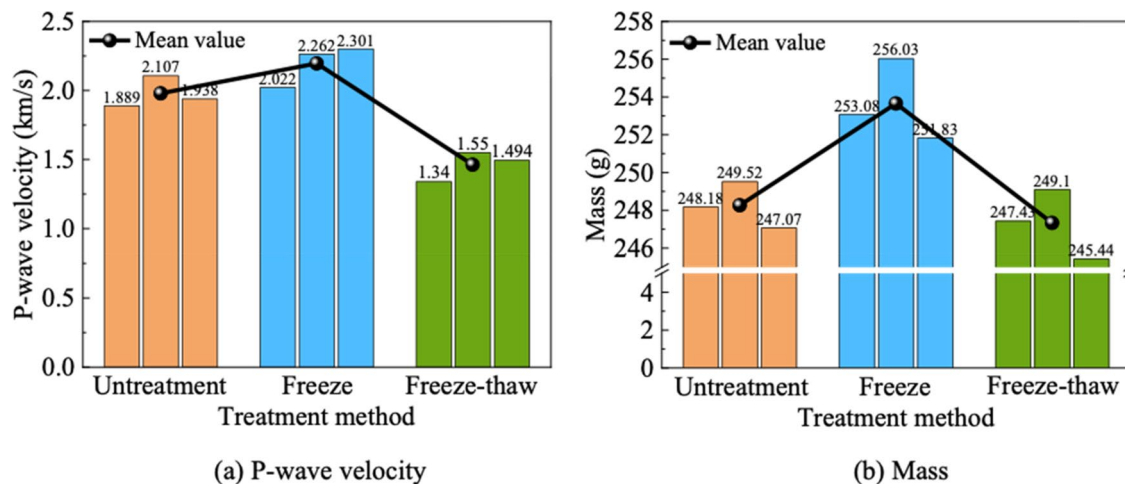


Fig. 4 Variation of the P-wave velocity and mass of the coal samples

thawing process. The result shows that the LN<sub>2</sub> freeze–thaw has a better cracking effect on the coal.

The P-wave velocity and mass of coal samples under three states are shown in Fig. 4. Compared with the untreated coal sample, the P-wave velocity and mass of the freeze–thaw coal sample are reduced, especially the P-wave velocity, with an average decrease of about 26.14%. It is generally believed that there is a negative correlation between P-wave velocity and damage degree of rocks. It is worth noting that the P-wave velocity and mass of the frozen coal samples increase, and the average increase of the P-wave velocity is about 10.97%. During the freezing process, although many cracks are produced, the pores and cracks in the coal are filled with ice due to the phase transformation of free water and bound water in the coal sample (Qin et al. 2022), which will improve the P-wave conductivity. There may be two reasons for the mass increase of the frozen coal samples: residual LN<sub>2</sub> and frost forming on the surface of the frozen coal samples in the air. The decrease of the coal mass after the freeze–thaw is mainly due to the shedding of weakly cemented matrix particles under the action of the thermal shock load.

To further understand the damage characteristics of the coal caused by LN<sub>2</sub> thermal shock, the microscopic structure changes inside the coal samples are observed. Since it is hard to observe the micro-structure of the frozen coal, the SEM experiments of the untreated and freeze–thaw coal samples are carried out in this study. Considering the different temperature gradients at different positions of the coal sample during LN<sub>2</sub> thermal shock, samples are taken at two locations of the freeze–thaw coal sample, one on the surface of the coal sample and the other in the center of the coal sample. The results are shown in Fig. 5. At the magnification of 200 times, there was no obvious crack in the untreated sample. However, the obvious thermal cracks in the center and surface locations of the freeze–thaw coal sample are found, and the larger crack width is induced in the coal surface. At the 1000- and 3000-times magnification, there are obvious cracks in all samples. The initial cracks of the untreated samples are relatively straight, while the obvious intergranular crack and trans-granular crack are generated on the center and surface locations of the freeze–thaw coal samples, respectively. Compared with intergranular failure, trans-granular failure is more difficult to produce, indicating that the damage caused by the LN<sub>2</sub> treatment of the coal is not uniformly distributed in space, and the damage degree of the coal matrix that first contacts LN<sub>2</sub> is larger. The coal matrix after the freeze–thaw shows a scaly surface, and many crack tips are presented in the surface microstructure of the coal sample. At the magnification of 6000 times, the untreated sample has no

obvious cracks, and the coal matrix morphology is flat. In the center location of the freeze–thaw coal sample, the micro-cracks and pore damage caused by the tensile failure of the coal matrix can be observed. The number and size of micro-cracks further increase in the surface location of the freeze–thaw coal sample. The results indicate that the internal structures of the coal samples after the LN<sub>2</sub> treatment are improved to a large extent, which may lead to the change of mechanical properties and failure characteristics of the coal. The damage induced by LN<sub>2</sub> freeze–thaw is different in the spatial distribution of the coal. The damage degree on the surface of the coal sample is greater than that in the center of the coal sample, which is mainly because the thermal shock loading on the sample surface is the largest.

### 3.2 Mechanical Properties

The loading curves in the mechanical experiments are presented in Fig. 6. Figure 6a shows the stress–strain curves of the coal samples under three states in the uniaxial compression experiment, they can be roughly divided into four stages: compaction, elasticity, yield, and failure. In the compaction stage, the average strain of the untreated coal sample, frozen coal sample, and freeze–thaw coal sample is 0.0039, 0.0023, and 0.0042, respectively. Compared with the untreated coal sample, the compaction stage of the frozen coal sample is shortened obviously, while the compaction stage of the freeze–thaw coal sample is increased. Since there are free water and bound water in the coal, the ice can be observed on the surfaces of the frozen coal samples. Hence, the internal pores and cracks inside the frozen coal sample can be also filled with ice, thus, the open space is reduced. However, the internal open space of the freeze–thaw coal sample increases due to the increase of pore size and the generation of cracks, further resulting in the increase of compressibility. After entering the elastic stage, the stress response sensitivity of the coal samples under the three states is also different, and their stress response sensitivity is in order: frozen state > untreated state > freeze–thaw state. In the three states, the plastic yield stage of the frozen coal sample is the most obvious, and it rises in a jagged way. During the freezing process, the microcracks can be produced inside the coal, while the stiffness of the coal matrix increases. Therefore, under an external load, the crack initiation positions and the required stress of the matrix crack propagation increase. When the crack propagation encounters the pretreatment crack, a local stress concentration region will be generated, which will accelerate the crack propagation. Once the crack propagation reaches the coal matrix, the load required for the crack propagation increases again. Thus, a serrated load curve is formed in the yield stage. In the failure stage, the untreated

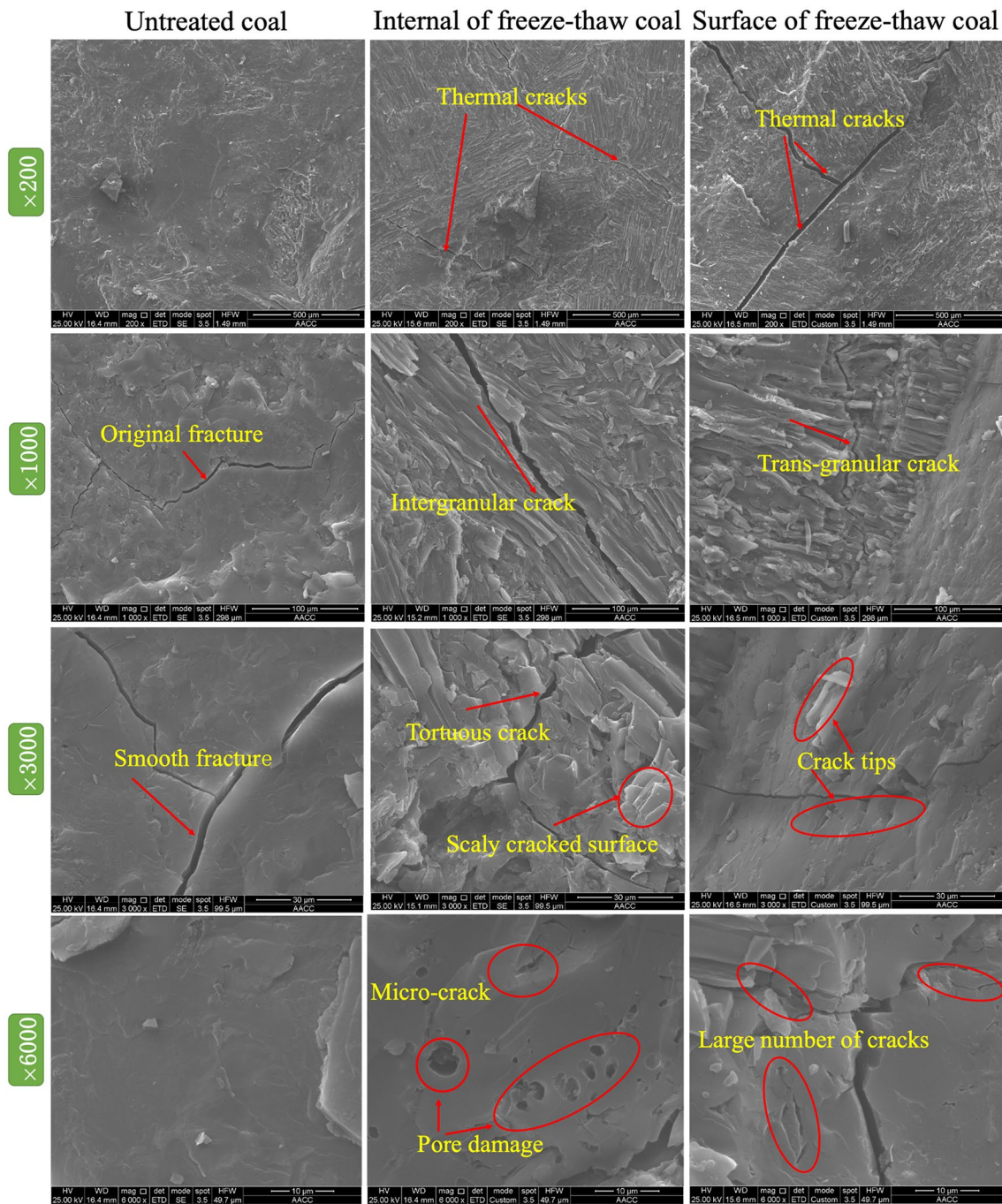
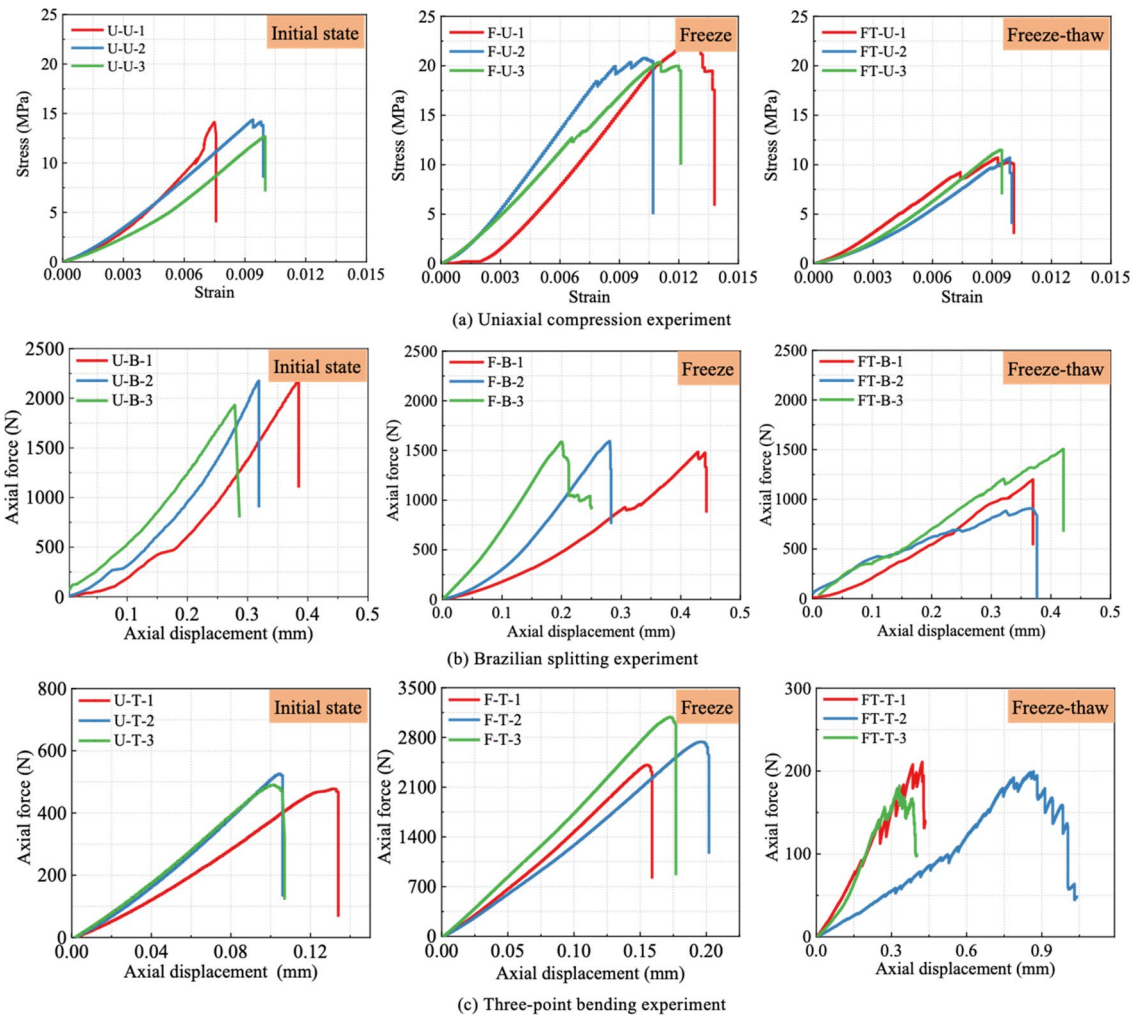


Fig. 5 Micro-structure characteristics of the coal samples

coal sample almost falls from the peak stress. The stress of the frozen coal sample decreases step by step, and its peak strain increases obviously. The freeze–thaw coal sample also presents similar results in the failure stage with the frozen coal sample, but the curve fluctuation is not so strong.

Figure 6b shows load–displacement curves of coal samples with different states under the Brazilian splitting tests. The loading curves of the untreated coal samples are smooth,

and brittle failure occurs. The load–displacement curves of the frozen coal samples have obvious inflection points before the failure, indicating that multistage crack propagations are present inside the samples. The smoothness of the loading curves of the freeze–thaw coal samples decreases greatly, which indicates that there are many defects induced by the freeze–thaw treatment inside the coal. During the loading process, the damage regions promote each other, resulting



**Fig. 6** Loading curves in the mechanical experiments

in the decrease of the cohesion between matrix particles and the gradual decrease of bearing capacity.

The load–displacement curves of the coal samples with different states in the three-point bending tests are shown in Fig. 6c. It can be found that the load–displacement curve shapes of both the untreated and frozen coal samples are relatively smooth, the peak load and axial displacement of the coal sample significantly increase after the freeze treatment. However, the loading curves of the freeze–thaw coal samples present a distinct jagged shape near the failure, and the maximum load decreases and axial displacement increases obviously. It is shown that the crack propagation path is complex during the loading process, and the damage induced by the LN<sub>2</sub> freeze–thaw affects the crack propagation.

Through the calculation, the compressive strength and elastic modulus of coal samples in three states are shown in Fig. 7a, b respectively. Compared with the untreated coal samples, the compressive strength and elastic modulus of

the frozen coal samples increase by 52.85 and 38.76% on average, respectively. While the compressive strength and elastic modulus of the freeze–thaw coal samples decrease by 21.20 and 23.20%, respectively. The tensile strength and fracture toughness of the coal samples with different states are shown in Fig. 7c, d, respectively. It can be found that the tensile strength of the coal in the three states is arranged from high to low: untreated state, frozen state, and freeze–thaw state. Compared with the untreated coal sample, the tensile strength of the frozen and freeze–thaw coal samples decreases by 26.17 and 42.99% on average, respectively. By the freeze treatment, the fracture toughness of the coal sample increases by 495.07%, while the fracture toughness of the coal samples through freeze–thaw treatment decreased obviously by 58.33%.

According to the above results, the influence of the LN<sub>2</sub> cooling state on the mechanical properties of the coal is very significant. Although cracks occur in the frozen coal samples, the stiffness of the coal matrix becomes also greater



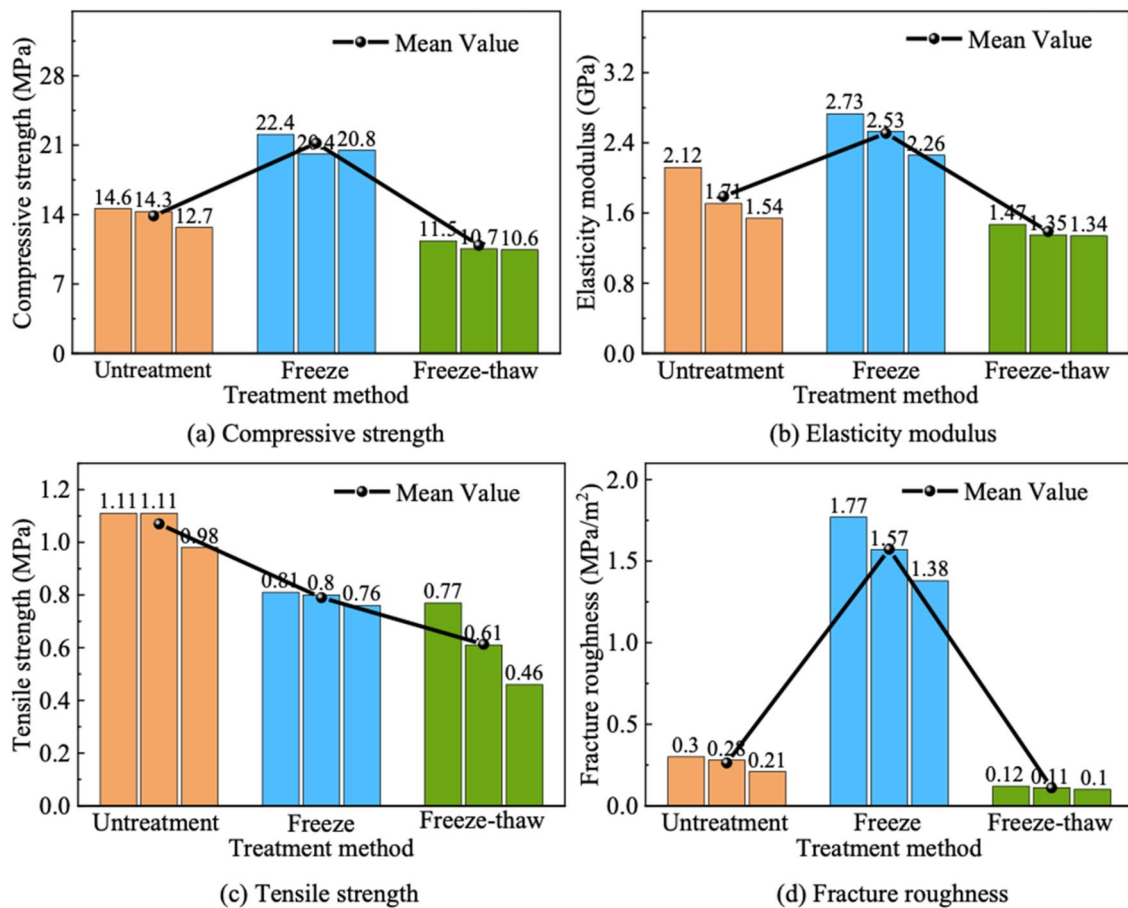


Fig. 7 Mechanical parameters of the coal samples

due to the action of the freezing. The former can increase the crack initiation positions, while the latter can increase the compressive strength of the frozen coal sample and the stress required for the matrix crack initiation and propagation. As a result, the compressive strength, elastic modulus, and fracture toughness of the frozen coal sample show an obvious increase. Compared with the increase of the coal matrix stiffness, the generated cracks inside the frozen coal sample are more sensitive to the tensile stress, so its tensile strength decreases. Under the action of two thermal shocks of cooling and rewarming, the structure of the freeze–thaw coal sample is seriously damaged, the damaged area and damage degree will be further increased compared with a single freezing process. Hereby, the cohesion of the internal structure of the freeze–thaw coal sample will be greatly weakened. Naturally, all mechanical characteristic parameters are weakened.

### 3.3 Fracture Propagation Characteristics

During the process of rock failure, the energy gathered inside the rock will be released in the form of elastic waves

due to the initiation, development, and expansion of micro-cracks. This phenomenon is called the AE phenomenon (Du et al. 2020a). Therefore, the AE can be used to qualitatively analyze the evolution process of rock internal cracks.

The variations in the ringing count of the AE under the uniaxial compression of the coal samples are shown in Fig. 8. The ringing count of the untreated coal presents a significant sudden increase, where the ring count is in a relatively low active state before the failure and becomes extremely active near the failure. After the LN<sub>2</sub> treatment, the frequency of the ringing count events increases significantly during the compression and elastic stages, while the magnitude of the ringing count has an obvious reduction near the failure. It can be also observed that the frequency of the ringing count events of the freeze–thaw coal is greater than that of the frozen coal. For the ring count distribution above the blue dotted line, both the event and magnitude of the ringing count of the frozen coal before the failure are larger than that of the freeze–thaw coal. At the failure stage, the ringing count of the freeze–thaw coal shows a small sharp increase, while this phenomenon has not been presented for the frozen coal. There is a positive correlation

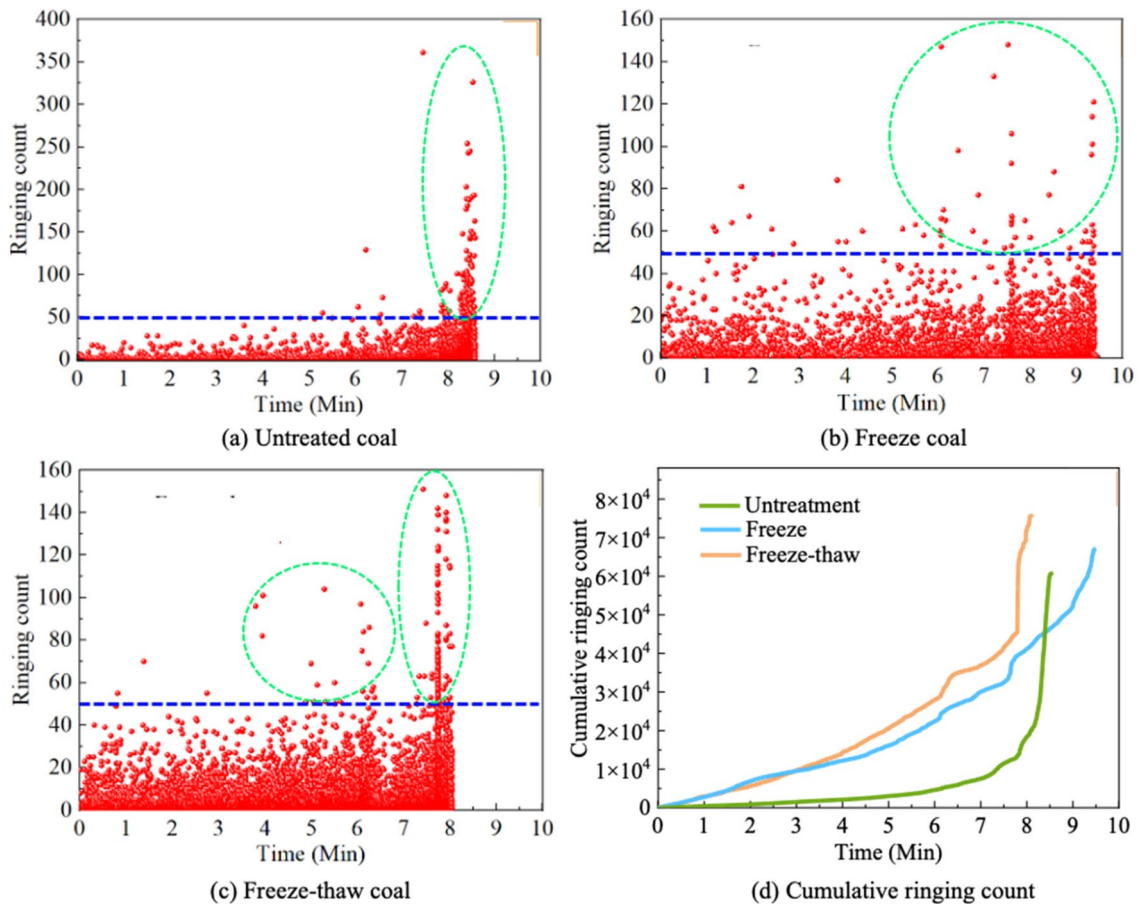


**Fig. 8** Changes in the AE ringing count of the coal during the uniaxial compression. For comparison, the blue dotted line represents the same level of ringing count, which has a value of 50

between the ring count and crack propagation. The damage caused by the  $\text{LN}_2$  treatment leads to the increase of microcracks inside the coal, and then the initiation and propagation activities of the cracks are enhanced under the action of the external loading, where the more serious the damage is, the higher the crack activity is. As the pretreatment microcracks in the frozen coal samples continue to expand, the AE becomes active. However, at the same time, as the coal matrix becomes more brittle, in turn, it inhibits the propagation of cracks, and the cracks continue to expand only when the stress reaches a certain value. This is mainly the reason for the difference in the AE between the frozen coal and frozen–thaw coal under the uniaxial compression test. Based on the change of cumulative ringing count, the AE of the untreated coal increases suddenly in a short time, showing brittle failure characteristics. The development of internal cracks for the treated coal always maintains a high activity, showing a certain ductility failure. The ductility characteristics of the freeze–thaw coal are more obvious compared with the frozen coal. Due to the increase of both cracks and matrix brittleness inside the frozen coal, the frozen coal

sample shows a special failure behavior of the brittleness and ductility at the same time.

Based on the AE information, the distribution characteristics between rise time/amplitude (RA) and AE counts/duration (AF) are often employed to determine the classification of tensile and shear cracks (Ohtsu et al. 1998). In general, the propagation process of tensile cracks inside rocks corresponds to high AF values and low RA values, while shear cracks are characterized by high RA values and low AF values (Lu et al. 2021). As shown in Fig. 9, the relationship between AF and RA, namely,  $\text{AF} = 0.037 \times \text{RA}$  is taken as a boundary between tensile and shear cracks under different cases. The proportions of tensile and shear fractures in the uniaxial compression experiments are summarized in Table 1. As shown in Table 1, the average proportion of shear fractures of the untreated coal, frozen coal, and freeze–thaw coal is 37.6%, 59.9%, and 65.8%, respectively. The shear crack becomes more active after  $\text{LN}_2$ -cooling, and the proportion of shear fractures after  $\text{LN}_2$  freeze–thaw is the largest with an increase of 75.0% compared with the untreated coal. With the development of the  $\text{LN}_2$ -cooling

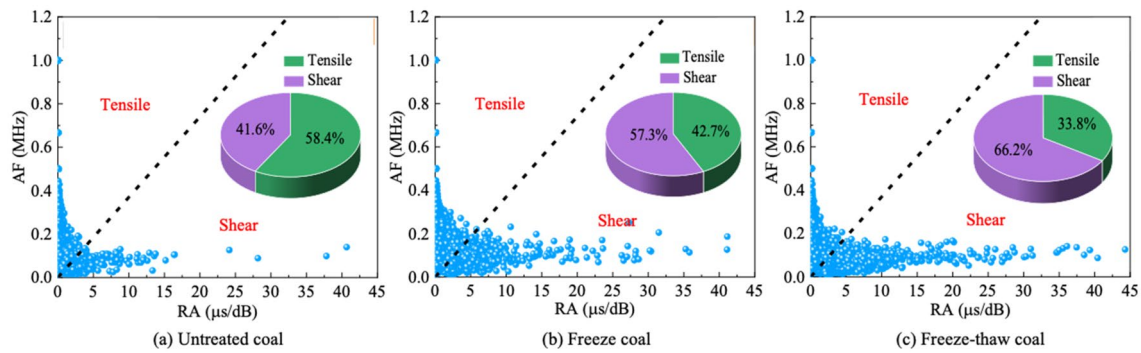


**Fig. 9** Crack classification through the RA–AF correlation distribution

**Table 1** Proportion of tensile and shear fractures in the uniaxial compression experiments

State	Sample no	Tensile (%)	Shear (%)
Untreated state	U-U-1	58.4	41.6
	U-U-2	62.7	37.3
	U-U-3	66.1	33.9
Freeze state	F-U-1	42.7	57.3
	F-U-2	36.5	63.5
	F-U-3	41.0	59.0
Freeze–thaw state	FT-U-1	40.2	59.8
	FT-U-2	33.8	66.2
	FT-U-3	28.7	71.3

state, more micro-fractures are induced by thermal shock, and then the number of shear fractures under uniaxial compression stress also becomes larger. Compared with the untreated coal, LN<sub>2</sub>-cooling can reduce cementation degree between mineral particles, and it is easy to cause unsteady slip propagation along the pretreated crack. Therefore, there are many shear failures from micro-fractures formed inside coal samples after the freeze–thaw treatment.

### 3.4 Failure Mode

The morphology and distribution of the macroscopic cracks after the coal failure have an important reference role in studying the formation of the crack network during the reservoir fracturing, and the structural characteristics of the crack network have a direct impact on the exploitation efficiency of CBM. Therefore, the experimental study on the failure characteristics of the coal samples with different states can better provide relevant guidance for the LN<sub>2</sub> fracturing of coal seams. Figure 10 shows the failure modes of the coal samples.

Under the uniaxial compression, the failure of the untreated coal samples is dominated by a single main fracture surface, and meanwhile, some secondary cracks are

generated. Most cracks are parallel to the direction of the axial load, which indicates that the failure process is mainly controlled by the tensile stress. The coal samples after the destruction are relatively complete, accompanied by a small number of fragments. The frozen coal samples are seriously damaged with no main fracture surface, and many fragments from the surface of the coal samples during the loading process peel off. The fracture surface is very rough, in which there are a lot of secondary cracks. The failure model of the freeze–thaw coal samples is similar to the frozen coal samples. The coal sample was almost destroyed, and a lot of debris is formed. As to the freeze and freeze–thaw coal sample, the crack propagation process is disordered under uniaxial compression due to the existence of quite a few pre-cracks induced by the LN<sub>2</sub> cooling. The cracks are more likely to grow along the pre-cracks, and the crack growth mode also becomes more complex.

In the Brazilian splitting experiment, it can be found that the untreated coal sample is a typical tensile failure. The crack is destroyed from the center point and runs through the coal sample, forming a single main crack without any redundant branch cracks. The crack propagation path of the frozen coal samples is relatively complex, and there are many small branch cracks near the main crack. As to the freeze–thaw coal samples, several main cracks and some branch cracks appear. The branch cracks and the main cracks are connected in series, which forms a considerable damage effect. In the three states, the freeze–thaw coal samples have the greatest crack growth, indicating that the pre-cracks of the freeze–thaw coal are larger than that of the frozen coal.

In the three-point bending test, the untreated coal samples present a typical tensile failure. The crack expands along the artificial crack to the loading point, and the induced crack is relatively flat and smooth. Compared with the untreated coal samples, the crack propagation path of the frozen coal samples becomes tortuous, and the concavity of the fracture surface morphology increases. The crack extension path of the freeze–thaw coal sample is the most tortuous, and there is obvious steering in the crack propagation process. After

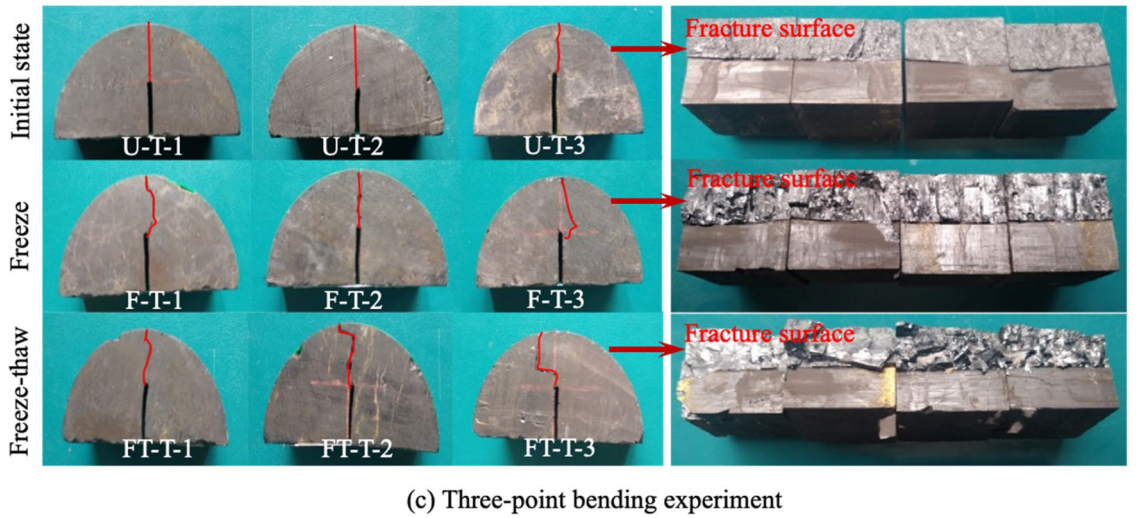
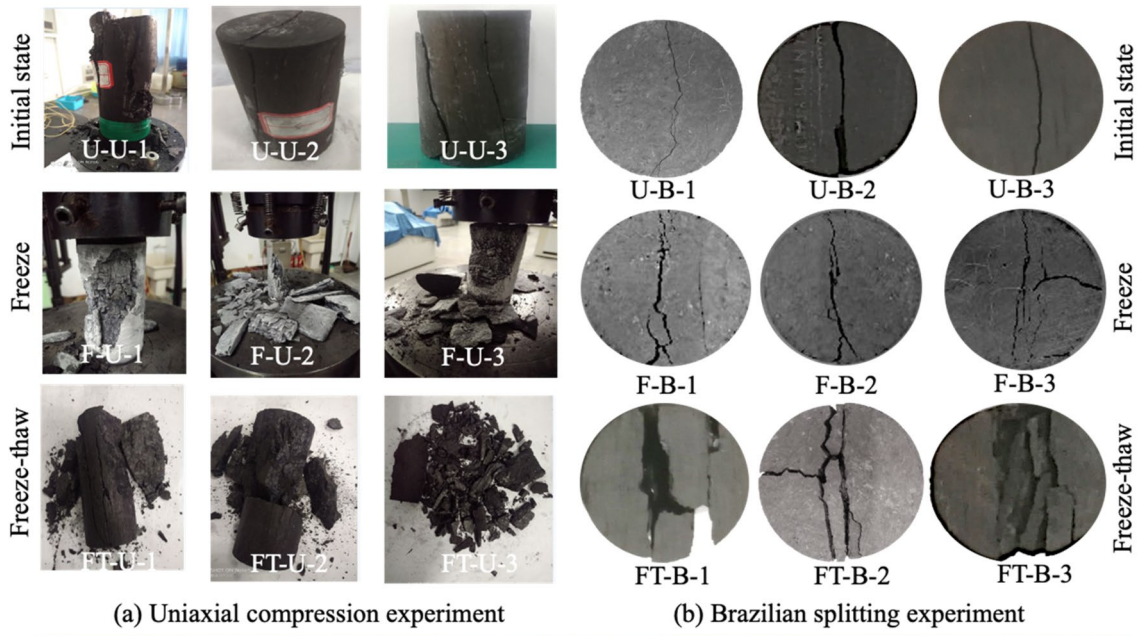


Fig. 10 Failure modes of the coal samples

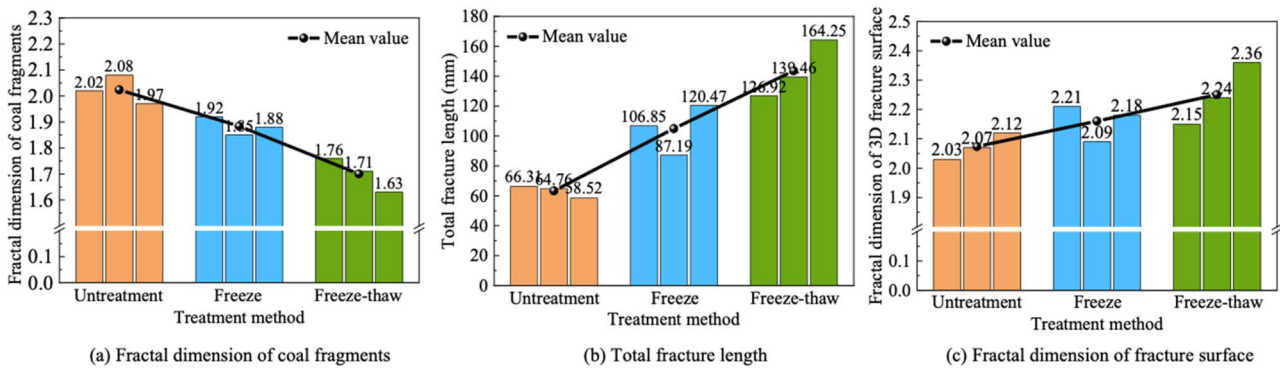


Fig. 11 Fracture parameters of the coal samples

the freeze–thaw treatment, the roughness degree of the 3D fracture surface is also the largest. Obviously, the more pre-cracks inside coal samples, the more turning opportunities of crack propagation, further resulting in the more tortuous the crack profile and the rougher the crack surface.

To quantitatively analyze crack morphology, the characteristic parameters of the fracture modes are shown in Fig. 11. After the coal sample is destroyed, different size fragments are formed. Fractal theory can be used to describe the distribution characteristics of rock fragments, and the fractal dimension can be calculated based on the mass, quantity, and size of fragments. The fractal dimension of the coal fragments after the uniaxial compression experiments is shown in Fig. 11a. The larger the fractal dimension is, the larger the span between adjacent fragment sizes is, and there are fewer fragments between the largest fragment and the smallest fragment. Therefore, in this case, the crack network is mainly composed of main cracks, and the branch cracks are few, so it is difficult to form a complex crack network. On the contrary, the smaller the fractal dimension is, the more uniform the debris size distribution is, and the smaller the size difference is. Therefore, it is easy to form a complex "tree-like" fracture network. The experimental results show that the fractal dimension of the coal fragments has a significant reduction trend with the development of the LN<sub>2</sub> cooling state, and the high-volume rupture is induced after the freeze–thaw treatment. As shown in Fig. 11b, the total fracture length of the coal in the three states under the Brazilian splitting experiments is arranged from low to high: untreated state, frozen state, and freeze–thaw state. The fractal dimension of the 3D fracture surface in the three states under the three-point bending test also has a similar trend. In a word, the complexity of the induced crack in the mechanical tests of the coal increases after the LN<sub>2</sub>-cooling pre-treatment, especially the freeze–thaw coal sample which has experienced two thermal shocks. LN<sub>2</sub> thermal shock can effectively stimulate the damage potential of initial defects in coal. Under the action of external force, these induced micro-cracks gradually expand, resulting in more damage areas and more complex crack morphology.

### 4 Thermal Damage Mechanism

In the process of the LN<sub>2</sub> thermal shock, the initiation and propagation of cracks in rocks are closely related to the heat transfer mechanism and mineral distribution. To explain the change of the fracturing behavior of the coal under three states, the micro-fracture mechanism of the coal during the LN<sub>2</sub> freeze–thaw is quantitatively evaluated and

discussed in this section based on the thermo-mechanical coupling phase-field model.

#### 4.1 Thermo-mechanical Coupling Phase-Field Model

Heat transfer of LN<sub>2</sub> thermal shock in the coal is governed by a thermal diffusion equation (Liu et al. 2020a):

$$\nabla(k\nabla T) + Q = \rho c_p \frac{\partial T}{\partial t}, \tag{3}$$

where  $t$  is the time,  $T$  is the temperature,  $Q$  is the heat source,  $c_p$  is the heat capacity,  $\rho$  is the density of the coal, and  $k$  is the heat conductivity.

The thermal boundary is as follows:

$$\begin{cases} T = \bar{T} \rightarrow \partial\Omega_D \\ \mathbf{n}^T \cdot (-k\nabla T) = \bar{Q} + h(T - \bar{T}) \rightarrow \partial\Omega_N, \end{cases} \tag{4}$$

where  $\bar{T}$  is the specified boundary temperature,  $h$  is the convective parameter of heat exchange,  $\bar{Q}$  is the specified boundary heat source, and  $\mathbf{n}^T$  is the normal unit vector.

The mechanical equation of the coal is given as follows:

$$0 = \nabla \cdot \boldsymbol{\sigma} + \mathbf{F}_V, \tag{5}$$

where  $\boldsymbol{\sigma}$  is the stress tensor,  $\mathbf{F}_V$  is the volumetric force tensor and it is zero in this study.

The stress tensor is given based on Duhamel–Hooke’s law:

$$\boldsymbol{\sigma} = \mathbf{D} : \boldsymbol{\varepsilon}^e(\mathbf{u}, T) \tag{6}$$

where  $\mathbf{D}$  is the elasticity modulus tensor,  $\mathbf{u}$  is the displacement tensor, “:” denotes the double-dot tensor product. Assume that the coal is a linear thermo-elastic material, then the elastic strain  $\boldsymbol{\varepsilon}^e$  can be calculated by the difference between the linearly elastic strain and thermal strain  $\boldsymbol{\varepsilon}^{th}$ :

$$\boldsymbol{\varepsilon}^e = \frac{1}{2}[(\nabla\mathbf{u})^T + \nabla\mathbf{u}] - \boldsymbol{\varepsilon}^{th}. \tag{7}$$

The thermal strain can be expressed as follows:

$$\boldsymbol{\varepsilon}^{th} = \boldsymbol{\alpha}_T(T - T_0), \tag{8}$$

where  $T_0$  is the reference temperature,  $\boldsymbol{\alpha}_T$  is a thermal expansion tensor.

In the phase-field model, the essence of the crack propagation is the minimization process of the total Lagrange energy functional that is equal to the difference between the total kinetic energy and total potential energy (Liu et al. 2020a; Nguyen et al. 2019). By the calculation, the phase-field equation can be expressed as follows:

$$\frac{\partial d(\phi)}{\partial \phi} H_d - \phi + l_{int}^2 \nabla^2 \phi = 0, \tag{9}$$

where  $\phi$  is the phase field,  $d(\phi)$  is the damage function,  $l_{int}$  is the internal length scale that characterizes the width of the discrete fracture. The phase-field boundary is  $-\nabla \phi \cdot \mathbf{n} = 0 \rightarrow \partial \Omega_N$ . By selecting Power-law, the damage function  $d(\phi)$  is defined as

$$d(\phi) = 1 - (1 - \phi)^m, \tag{10}$$

where  $m = 2$  means that a quadratic function is employed.  $H_d$  is a state variable function that characterizes the local history strain field, and it depends on the crack driving force  $D_d$  (Liu et al. 2020a):

$$H_d(t, \mathbf{u}) = \max_{\tau \in [0, t]} D_d(\tau, \mathbf{u}). \tag{11}$$

The crack driving force is a function of the elastic strain energy density, and it can be defined as

$$D_d = \frac{l_{int}}{G_c - G_{c0}} \langle W_{s0}^+ - \frac{G_{c0}}{l_{int}} \rangle, \tag{12}$$

where  $G_c$  is the critical energy release rate,  $G_{c0}$  is the strain energy threshold and it is set as zero in this study,  $W_{s0}^+$  is the tensile part of the undamaged elastic strain energy density and its expression is given based on the spectral decomposition of the elastic strain tensor:

$$W_{s0}^+ = \frac{1}{2} \boldsymbol{\sigma}^+ : \boldsymbol{\epsilon}_{el}^+. \tag{13}$$

The tensile part of the elastic strain tensor  $\boldsymbol{\epsilon}_{el}^+$  can be given:

$$\boldsymbol{\epsilon}_{el}^+ = \sum_{i=1}^3 \boldsymbol{\epsilon}_{el, pi} \mathbf{n}_i \otimes \mathbf{n}_i, \tag{14}$$

where  $\boldsymbol{\epsilon}_{el, pi}$  is the principal value of the elastic strain tensor, and  $\mathbf{n}_i$  is the direction vector.

The tensile part of the undamaged stress tensor can be defined as

$$\boldsymbol{\sigma}^+ = \mathbf{C} : \boldsymbol{\epsilon}_{el}^+, \tag{15}$$

where  $\mathbf{C}$  is the 4th order elasticity tensor.

In the thermal diffusion equation, the thermal conductivity  $k$  depends on the crack phase-field  $\phi$  (Nguyen et al. 2019):

$$k = k_0 [\xi(g(\phi) - 1) + 1], \tag{16}$$

where  $k_0$  is the initial thermal conductivity,  $\xi$  is set as 1 in this study assuming no heat flow through cracks,  $g(\phi)$  is the stiffness weakening function and it is given:

$$g(\phi) = (1 - \delta)(1 - \phi)^2 + \delta, \tag{17}$$

where  $\delta$  is a parameter that is employed to avoid the numerical singularity in the simulation when  $\phi$  is close to 1.

Since the coal is assumed as the linear elastic material, the elasticity tensor  $\mathbf{D}$  also needs to be updated using the phase-field  $\phi$  (Liu et al. 2019):

$$\mathbf{D} = \mathbf{D}_0 [(1 - \delta)(1 - \phi)^2 + \delta], \tag{18}$$

where  $\mathbf{D}_0$  is the initial elasticity modulus tensor.

In addition, the critical energy release rate  $G_c$  in the plane strain condition can be expressed by the fracture toughness (Liu et al. 2019)

$$G_c = (1 - \nu^2) K_I^2 / E, \tag{19}$$

where  $\nu$  is the Poisson's ratio,  $E$  is the elastic modulus.

### 4.2 Model Implementation

Figure 12 shows the implementation process of the crack phase-field modeling. The coupled thermo-mechanical phase-field model mainly consists of the heat transfer equation, solid mechanics equation, local history strain equation, and phase-field equation, and they are independently solved through the segregated coupling solver. The thermal strain first is calculated by the heat transfer equation to update the solid mechanics' field. Then, the stress and strain are extracted and stored in the variable list. Subsequently, the strain energy density is calculated based on the called stress and strain values, and the local history strain field is updated. The updated  $H_d$  is applied to solve the crack phase field. In every step, the updated crack phase field is used to modify the thermal conductivity in the heat transfer equation and the elasticity tensor in the solid mechanics' equation. In this study, the Anderson acceleration is employed to accelerate the convergence process due to the low iterative convergence

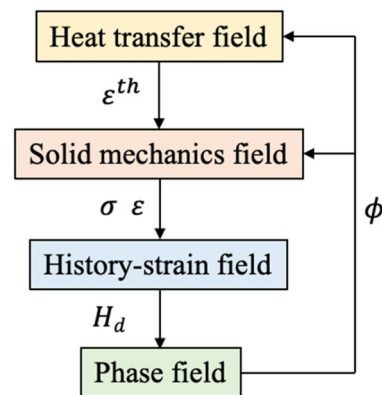


Fig. 12 Implementation process of the crack phase-field model

in the crack propagation, and the dimension of the iteration space is set as 60.

### 4.3 Model Verification

In this section, the quenching test of the ceramic slab is simulated to study the capability and accuracy of the thermo-mechanical coupling phase-field model in terms of modeling thermal cracking issues of brittle solids under thermal shock. According to the previous experiment study (Li et al. 2013), the ceramic slab first is heated to a specified temperature and then placed into a water bath at room temperature. Since an intensive temperature change occurs, the ceramic slab significantly shrank during the quenching test. As a result, many parallel and periodic fractures with different lengths are induced in the ceramic slab.

Considering the symmetry feature of the ceramic slab in the previous experiments, only half of the ceramic slab with a width of 10 mm and a length of 50 mm is used to simulate the quenching process. The plane strain condition is assumed in this study. In the crack phase-field model, the initiation and propagation of cracks are not only associated with the thermal shock degree and geometry of the model but also highly dependent on the finite element mesh and length scale parameter (Chu et al. 2017; Wang et al. 2020). Thus, the length scale parameter  $l_{\text{int}}$  is set as  $5 \times 10^{-2}$  mm that is typically small enough to ensure the number of the induced short cracks in the simulation, and the maximum element size  $h_{\text{max}} = l_{\text{int}}/2$  is applied. As a result, the geometry domain with the dimension of 10 mm  $\times$  25 mm is uniformly represented by 400,000 quadrilateral elements. The initial

temperature of the ceramic slab is set as 600 K before the quenching. The temperature of the water bath is maintained at 300 K. The thermal shock loads and mechanically free conditions are applied to the top, bottom, and left boundaries of the domain. The adiabatic condition and no normal displacement are assumed in the right boundary of the ceramic slab due to the symmetry of the domain. Meanwhile, the heat convection conditions are enforced on the top, bottom, and left boundaries of the domain. According to previous studies (Chu et al. 2017; Wang et al. 2018, 2020), the water seepage on fracture surfaces is neglected in this simulation due to no significant effect of the water flow on the thermal crack patterns. The other simulation parameters are list as follows (Wang et al. 2018):  $\alpha = 7.5 \times 10^{-6}$  1/K,  $c_p = 880$  J/(kg K),  $k_0 = 31.0$  W/(m K),  $h = 1.0 \times 10^4$  W/(m<sup>2</sup> K),  $\rho = 3980$  kg/m<sup>3</sup>,  $E = 370$  GPa,  $\nu = 1/3$ , and  $G_c = 42.47$  J/m<sup>2</sup>.

The comparison of the crack patterns among the previous experimental observation (Li et al. 2013), reported numerical results (Tang et al. 2016; Wang et al. 2018), and current numerical result is shown in Fig. 13. The current numerical result agrees reasonably well with both the previous experimental result and reported thermal crack patterns. The simulation result shows that a series of the periodic parallel short crack is first induced initiation, and then selective stagnation and propagation of the cracks are presented. The above phenomenon indicates that the cracking behaviors of the brittle ceramic slab during the quenching process can be captured by our model. Therefore, the capability and accuracy of our model in terms of dealing with thermal crack issues are qualitatively verified.

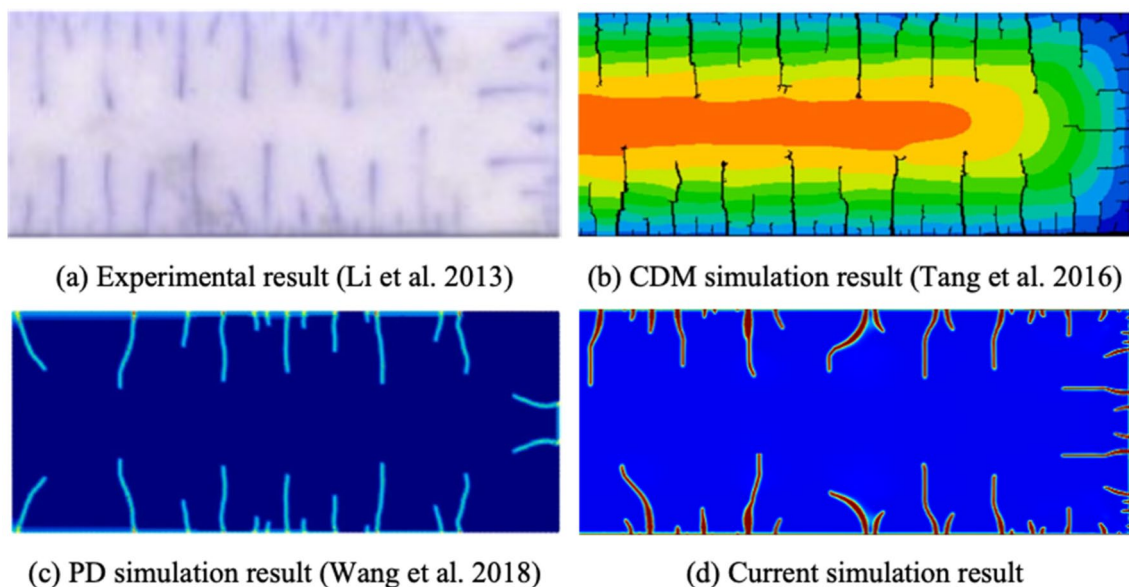


Fig. 13 Comparison of the fracture patterns obtained from different methods

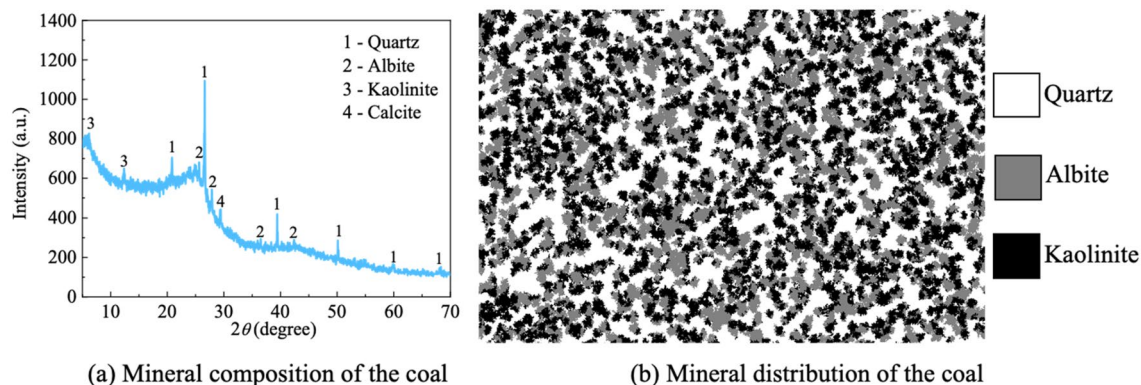


Fig. 14 Composition and distribution of minerals

#### 4.4 Reconstruction of Coal Matrix

To reconstruct the coal matrix at the micro-level, the X-ray diffraction experiment of the coal is first performed, and the result is shown in Fig. 14a. The mineral composition of the coal mainly contains quartz, albite, and kaolinite by the qualitative analysis, and a small amount of calcite is present. Therefore, the former three minerals are mainly considered in this study.

The coal matrix at the micro-scale is reconstructed by the quartet structure generation set (QSGS) proposed by Wang et al. (2007). In the QSGS method, the non-growing and growing phases need to be first determined. In general, the growth phase can be called the  $n$ th phase ( $2 \leq n \leq N$ ), where  $N$  is the total number of phases in the reconstruction model. Normally, discrete phases are often taken as the growth phases, and their growth process is presented as follows.

- (i) The growth cores in a grid system are defined by a distribution probability that is usually less than the volume fraction of the growth phase. The initial growth phases are randomly generated by the reformation of the growing core.
- (ii) The growth direction of each growth core is set as eight directions. The growing probability of each direction is specified, which can characterize the anisotropic feature of the reconstructed coal matrix.
- (iii) Repeat the step (ii) until the volume fraction of the growth phase reaches the specified value, and the growing process is performed.
- (iv) As to three or more growth phases in the reconstructed model, two cases need to be considered. If the current growth phase is a discrete phase, it corresponds to the existing growth phase. Then, its growth process is the same as the first growth phase, it can also be generated by steps (i)–(iii). Otherwise, the interaction between the next growth phase and the existing phase should be considered.

Table 2 Simulation parameters in the crack phase field model

Parameter	Quartz	Albite	Kaolinite
$\rho_s$ (kg/m <sup>3</sup> )	2650	2620	2650
$E$ (GPa)	96.0	63.6	21.4
$\nu$ (1)	0.08	0.28	0.36
$K_I$ (MPa·m <sup>1/2</sup> )	0.24	0.78	0.10
$G_c$ (J/m <sup>2</sup> )	0.60	8.82	0.41
$\alpha_T$ (1/K)	$11.0 \times 10^{-6}$	$6.6 \times 10^{-6}$	$1.7 \times 10^{-6}$
$c_p$ (J/(kg·K))	700	794	945
$k_0$ (W/(m·K))	7.69	2.80	3.71
$h$ (W/(m <sup>2</sup> ·K))	50	50	50
$\delta$ (1)	$1 \times 10^{-9}$	$1 \times 10^{-9}$	$1 \times 10^{-9}$

Based on the QSGS method, the reconstructed coal matrix is shown in Fig. 14b, where the white, gray, and black represent quartz, albite, and kaolinite, respectively. The size of the coal matrix is 1.12 mm × 0.84 mm. The proportion of the quartz, albite, and kaolinite is set as 40%, 32%, and 28%, respectively. The simulation parameters of each mineral used in the crack phase-field model are listed in Table 2, which are obtained from previous references (Christensen 1996; Dal Bo et al. 2013; Hulan and Stubna 2020; Lao et al. 2020; Linvill et al. 1984; Liu et al. 2020a; Michot et al. 2008; Sin et al. 2012; Tenner et al. 2007). The critical crack energy release rate values of minerals are calculated by Eq. (16).

#### 4.5 Simulation Results

The numerical simulation can not only accurately evaluate the local stress caused by the complex thermal history but also provide a method for studying the thermal crack process in detail. Thus, the coal matrix subjected to the freeze–thaw process is simulated in this section by the coupled thermo-mechanical phase-field method. The length scale parameter  $l_{int}$  is set as  $0.5 \times 10^{-2}$  mm, and the maximum element size



$h_{\max} = l_{\text{int}}/2$  is applied. As a result, the geometry domain is uniformly discretized by 150,528 quadrilateral elements. The initial temperature of the coal matrix is set as 298.15 K. The thermal shock loads shown in Eq. (20) and mechanically free conditions are applied to the four boundaries. To reduce the computational workload, the time boundaries of 10 and 16 s are selected based on the simulation experience, and the criterion of selection is that both temperature and damage are in equilibrium.

$$\begin{cases} \bar{T} = 77 \text{ K} & \text{if } t \leq 10 \text{ s} \\ \bar{T} = 298.15 \text{ K} & \text{if } 10 \text{ s} < t \leq 16 \text{ s} \end{cases} \quad (20)$$

The micro-crack initiation and propagation in the coal matrix during the LN<sub>2</sub> freeze–thaw process are shown in Fig. 15. The crack phase-field mainly concentrates at the region of the maximum tensile strain energy. It can be observed that cracks are mainly initiated and propagated in and around quartz grains. In the freezing process, some micro-cracks on the coal matrix are first generated when LN<sub>2</sub> is in contact with the surface of the coal matrix. With the increase in the freeze time, the typical trans-granular cracks can be found in quartz particles during the initiation of cracks, and the intergranular cracks also appear around some quartz grains. It is noted that thermal cracking is also easily induced in some edges and sharp corners of quartz particles because of the singularity of stress at these locations. With the passage of the freeze time, the temperature in the coal matrix becomes almost uniform, and the crack propagation rate obviously decreases. Therefore, the heterogeneity behaviors of mineral particles and temperature gradient cause cracks to occur randomly in the coal matrix. In the thawing process, the cracks continue to initiate and propagate, and the thermal cracking is much more active than the freezing process. However, this thermal cracking

process is very short. The main reason is that the thermal shock load will be significantly reduced when the temperature of the coal matrix is closer to the ambient temperature. In the thawing process, thermal cracking mainly comes from two aspects: the continuous propagation of previous cracks and the generation of new cracks. By comparing the microstructure changes of the coal between the experiment and numerical simulation during the LN<sub>2</sub> freeze–thaw, they have two obvious similarities. The first one is that the obvious structural damage including the generated microcracks and pore damage is induced by LN<sub>2</sub> freeze–thaw. The second one is that the damage of the coal surface structure is more serious than that of the coal internal structure, because the thermal stress induced by LN<sub>2</sub> is maximum at the initial contact surface between LN<sub>2</sub> and coal (Du et al. 2020b). The results not only further verify the effectiveness of the crack phase-field model but also make up for the lack of

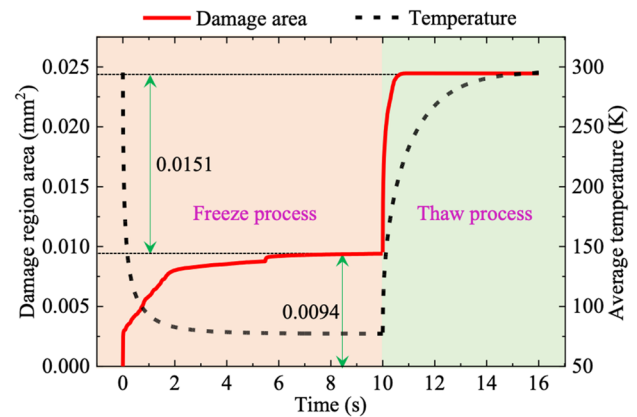


Fig. 16 Changes in the fracture region area and average temperature with time

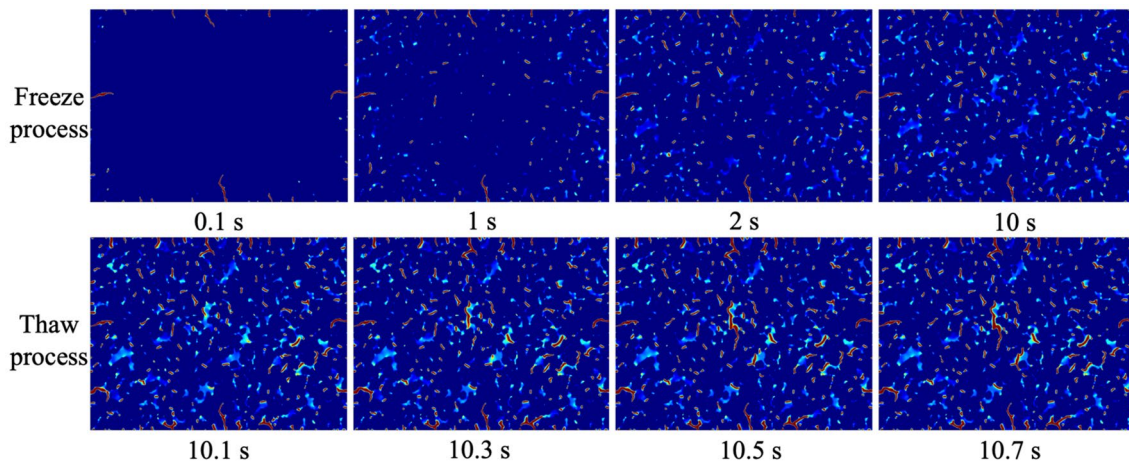


Fig. 15 Micro-crack initiation and propagation during the LN<sub>2</sub> freeze–thaw process (red: fracture, blue: coal matrix)

dynamic observation of microcrack evolution in the experimental process.

The evolution of the damage region area and average temperature over time are shown in Fig. 16. In this study, the damage region area is calculated by the sum of the local areas, where phase-field  $\phi$  is larger than 0.95. The temperature balance time of the coal matrix in both the freeze and thaw process is about 6 s. The changes in the damage region area with the increase in the freeze time presents a multi-stage, and it is closely related to the change of the temperature gradient. In the initial freeze stage, the growth rate of the damaged area is the largest because of a very large thermal shock loading induced by a rapid temperature change. The growth rate of the damage area decreases as the temperature gradient reduces. It can be also found that there is a small sudden increase in the damage region area after the temperature balance, which may be induced by the mismatch of the thermal stress between adjacent mineral particles. Although the temperature balance time between the freeze and thaw process is almost the same, the thermal cracking behavior in the thawing process occurs mainly in the first one second. The damage region area in this time reaches 0.0151 mm<sup>2</sup>, which is 1.61 times the damage area in the whole freezing process. The result indicates that the growth rate of the micro-cracks in the LN<sub>2</sub> thaw process is larger than that in the LN<sub>2</sub> freeze process. Based on the previous crack pattern analysis, we can find that the continuous propagation of cracks induced by the LN<sub>2</sub> freeze significantly accelerates the increase of the damage area.

By the numerical simulation of the thermal cracking process, the damage mechanism of the coal matrix during the freeze–thaw is revealed. From a temperature point of view, the damage of the coal in the LN<sub>2</sub> fracturing can be divided into two stages: freeze stage and thaw stage. The latter is often ignored, in fact, its contribution to the coal damage is the largest. The simulation results well explain the changes in the fracturing behavior of the coal under the three states in the mechanical experiments. The larger the initial damage in the coal samples is, the more crack propagation paths and the more complex the crack morphology are in the fracturing tests.

## 5 Conclusions

To study the effect of the LN<sub>2</sub>-cooling state on the mechanical properties and fracture characteristics of the coal, a series of laboratory experiments on the coal specimens with different LN<sub>2</sub> treatment methods is performed. The fracture mechanism of the coal subjected to LN<sub>2</sub>-cooling is revealed from microscale. The conclusions can be shown as follows:

1. Compared with the untreated coal sample, the P-wave velocity, compressive strength, elastic modulus, and fracture toughness of the frozen coal sample have been greatly increased by 10.97%, 52.85%, 38.76%, and 495.07%, respectively, while its tensile strength has been reduced by 26.17%. The P-wave velocity, compressive strength, elastic modulus, tensile strength, and fracture toughness of freeze–thaw coal samples decreased significantly, with an average decrease of 26.14%, 21.20%, 23.20%, 42.99%, and 58.33%, respectively. It indicates that the physical and mechanical properties of the freeze–thaw coal are deteriorating. The low-temperature freezing environment produced by LN<sub>2</sub> has a certain strengthening effect on the mechanical properties of coal.
2. At the micro-level, the damage of the coal induced by LN<sub>2</sub>-cooling is different in the spatial distribution. The damage of the coal surface is the largest, in which the trans-granular microcrack can be found and the number and size of micro-cracks also increase. After the LN<sub>2</sub>-cooling treatment, the failure mode, failure path, crack propagation direction, and fracture surface morphology of the coal in the mechanical experiment become more complex, in which the freeze–thaw coal samples have the best failure effect.
3. The thermal shock damage caused by LN<sub>2</sub>-cooling is mainly manifested in two aspects: temperature gradient inside the coal and mismatch of thermal stress between adjacent mineral particles due to the heterogeneity features of mineral particles. The damage region area in the LN<sub>2</sub> thawing process is 1.61 times that in the whole freezing process, and the growth rate of the micro-cracks in the LN<sub>2</sub> thawing process is also larger than that in the LN<sub>2</sub> freezing process. The LN<sub>2</sub> thawing process cannot be ignored. The above results can well explain the variations in the fracturing behaviors of the coal with different LN<sub>2</sub> treatment states in the mechanical experiments.

**Acknowledgements** This work had been financially supported by the National Natural Science Foundation of China (51604263, U1762105, and 51904270), the China Postdoctoral Science Foundation (2020M673451), the China University of Mining and Technology [3021802, The Fluidization Mining for Deep Coal Resources], and the Natural Science Foundation of Jiangsu Province (BK20160252).

**Author Contributions** PH, SS and FG conceived and designed the study. PH performed the numerical simulations and wrote the manuscript. SS, XL and SW carried out the experiment. SS and YG analyzed the experimental results. FG and CC edited this manuscript.

## Declarations

**Conflict of Interest** The authors declare that they have no conflict of interest.

## References

- Anderson RL, Ratcliffe I, Greenwell HC, Williams PA, Cliffe S, Coveney PV (2010) Clay swelling—a challenge in the oilfield. *Earth Sci Rev* 98:201–216. <https://doi.org/10.1016/j.earscirev.2009.11.003>
- Cai CZ, Gao F, Li GS, Huang ZW, Hou P (2016) Evaluation of coal damage and cracking characteristics due to liquid nitrogen cooling on the basis of the energy evolution laws. *J Nat Gas Sci Eng* 29:30–36. <https://doi.org/10.1016/j.jngse.2015.12.041>
- Cai CZ, Gao F, Yang YG (2018) The effect of liquid nitrogen cooling on coal cracking and mechanical properties. *Energ Explor Exploit* 36:1609–1628. <https://doi.org/10.1177/0144598718766630>
- Cha MS, Yin XL, Kneafsey T, Johanson B, Alqahtani N, Miskimins J, Patterson T, Wu YS (2014) Cryogenic fracturing for reservoir stimulation—laboratory studies. *J Petrol Sci Eng* 124:436–450. <https://doi.org/10.1016/j.petrol.2014.09.003>
- Christensen NI (1996) Poisson's ratio and crustal seismology. *J Geophys Res Sol Ea* 101:3139–3156. <https://doi.org/10.1029/95JB03446>
- Chu YP, Zhang DM (2019) Study on the pore evolution law of anthracite coal under liquid nitrogen freeze-thaw cycles based on infrared thermal imaging and nuclear magnetic resonance. *Energy Sci Eng* 7:3344–3354. <https://doi.org/10.1002/ese3.505>
- Chu DY, Li X, Liu ZL (2017) Study the dynamic crack path in brittle material under thermal shock loading by phase field modeling. *Int J Fracture* 208:115–130. <https://doi.org/10.1007/s10704-017-0220-4>
- Chu YP, Sun HT, Zhang DM, Yu G (2020) Nuclear magnetic resonance study of the influence of the liquid nitrogen freeze-thaw process on the pore structure of anthracite coal. *Energy Sci Eng* 8:1681–1692. <https://doi.org/10.1002/ese3.624>
- Coetzee S, Neomagus HWJP, Bunt JR, Strydom CA, Schobert HH (2014) The transient swelling behaviour of large (-20+16 mm) South African coal particles during low-temperature devolatilisation. *Fuel* 136:79–88. <https://doi.org/10.1016/j.fuel.2014.07.021>
- Dal Bo M, Cantavella V, Sanchez E, Hotza D, Gilabert FA (2013) Fracture toughness and temperature dependence of Young's modulus of a sintered albite glass. *J Non Cryst Solids* 363:70–76. <https://doi.org/10.1016/j.jnoncrysol.2012.12.001>
- Dong J, Cheng YP, Jin K, Zhang H, Liu QQ, Jiang JY, Hu BA (2017) Effects of diffusion and suction negative pressure on coalbed methane extraction and a new measure to increase the methane utilization rate. *Fuel* 197:70–81. <https://doi.org/10.1016/j.fuel.2017.02.006>
- Du K, Li XF, Tao M, Wang SF (2020a) Experimental study on acoustic emission (AE) characteristics and crack classification during rock fracture in several basic lab tests. *Int J Rock Mech Min* 133:104411. <https://doi.org/10.1016/j.ijrmms.2020.104411>
- Du ML, Gao F, Cai CZ, Su SJ, Wang ZK (2020b) Study on the surface crack propagation mechanism of coal and sandstone subjected to cryogenic cooling with liquid nitrogen. *J Nat Gas Sci Eng* 81:103436. <https://doi.org/10.1016/j.jngse.2020.103436>
- Garcia VJ, Marquez CO, Zuniga-Suarez AR, Zuniga-Torres BC, Villalta-Granda LJ (2017) Brazilian test of concrete specimens subjected to different loading geometries: review and new insights. *Int J Concr Struct M* 11:343–363. <https://doi.org/10.1007/s40069-017-0194-7>
- Hou P, Gao F, Gao YN, Yang YG, Cai CZ (2018) Changes in breakdown pressure and fracture morphology of sandstone induced by nitrogen gas fracturing with different pore pressure distributions. *Int J Rock Mech Min* 109:84–90. <https://doi.org/10.1016/j.ijrmms.2018.06.006>
- Hou P, Liang X, Gao F, Dong JB, He J, Xue Y (2021a) Quantitative visualization and characteristics of gas flow in 3D pore-fracture system of tight rock based on lattice Boltzmann simulation. *J Nat Gas Sci Eng* 89:103867. <https://doi.org/10.1016/j.jngse.2021.103867>
- Hou P, Liang X, Zhang Y, He J, Gao F, Liu J (2021b) 3D multi-scale reconstruction of fractured shale and influence of fracture morphology on shale gas flow. *Nat Resour Res* 30:2463–2481. <https://doi.org/10.1007/s11053-021-09861-1>
- Hou P, Su SJ, Liang X, Gao F, Cai CZ, Yang YG, Zhang ZZ (2021c) Effect of liquid nitrogen freeze-thaw cycle on fracture toughness and energy release rate of saturated sandstone. *Eng Fract Mech* 258:108066
- Hou P, Xue Y, Gao F, Dou FK, Su SJ, Cai CZ, Zhu CH (2022) Effect of liquid nitrogen cooling on mechanical characteristics and fracture morphology of layer coal under Brazilian splitting test. *Int J Rock Mech Min* 151:105026
- Hulan T, Stubna I (2020) Young's modulus of kaolinite-illite mixtures during firing. *Appl Clay Sci* 190:105584. <https://doi.org/10.1016/j.clay.2020.105584>
- Jin XM, Gao JL, Su CD, Liu JJ (2019) Influence of liquid nitrogen cryotherapy on mechanic properties of coal and constitutive model study. *Energy Source Part A* 41:2364–2376. <https://doi.org/10.1080/15567036.2018.1563245>
- Lao XB, Xu XY, Jiang WH, Liang J, Miao LF, Wu Q (2020) Influences of impurities and mineralogical structure of different kaolin minerals on thermal properties of cordierite ceramics for high-temperature thermal storage. *Appl Clay Sci* 187:105485. <https://doi.org/10.1016/j.clay.2020.105485>
- Li J, Song F, Jiang CP (2013) Direct numerical simulations on crack formation in ceramic materials under thermal shock by using a non-local fracture model. *J Eur Ceram Soc* 33:2677–2687. <https://doi.org/10.1016/j.jeurceramsoc.2013.04.012>
- Li H, Lin BQ, Chen ZW, Hong YD, Zheng CS (2017) Evolution of coal petrophysical properties under microwave irradiation stimulation for different water saturation conditions. *Energy Fuel* 31:8852–8864. <https://doi.org/10.1021/acs.energyfuels.7b00553>
- Li B, Ren YJ, Lv XQ (2020a) The evolution of thermal conductivity and pore structure for coal under liquid nitrogen soaking. *Adv Civ Eng* 2020:2748092. <https://doi.org/10.1155/2020/2748092>
- Li HW, Zuo JP, Wang LG, Li PF, Xu XW (2020b) Mechanism of structural damage in low permeability coal material of coalbed methane reservoir under cyclic cold loading. *Energies* 13:519. <https://doi.org/10.3390/en13030519>
- Liang X, Hou P, Xue Y, Yang XJ, Gao F, Liu J (2021a) A fractal perspective on fracture initiation and propagation of reservoir rocks under water and nitrogen fracturing. *Fractals* 29(7):2150189. <https://doi.org/10.1142/S0218348X21501899>
- Liang X, Hou P, Yang XJ, Xue Y, Teng T, Gao F, Liu J (2021b) On estimating plastic zones and propagation angles for mixed mode I/II cracks considering fractal effect. *Fractals*. <https://doi.org/10.1142/S0218348X22500116>
- Liew MS, Danyaro KU, Zawawi NAWA (2020) A comprehensive guide to different fracturing technologies: A review. *Energies* 13:3326. <https://doi.org/10.3390/en13133326>
- Lim IL, Johnston IW, Choi SK (1993) Stress intensity factors for semicircular specimens under 3-point bending. *Eng Fract Mech* 44:363–382. [https://doi.org/10.1016/0013-7944\(93\)90030-V](https://doi.org/10.1016/0013-7944(93)90030-V)
- Linville ML, Vandersande JW, Pohl RO (1984) Thermal-conductivity of feldspars. *B Mineral* 107:521–527

- Liu DM, Yao YB, Tang DZ, Tang SH, Che Y, Huang WH (2009) Coal reservoir characteristics and coalbed methane resource assessment in Huainan and Huaibei coalfields, Southern North China. *Int J Coal Geol* 79:97–112. <https://doi.org/10.1016/j.coal.2009.05.001>
- Liu ZD, Cheng YP, Dong J, Jiang JY, Wang L, Li W (2018) Master role conversion between diffusion and seepage on coalbed methane production: implications for adjusting suction pressure on extraction borehole. *Fuel* 223:373–384. <https://doi.org/10.1016/j.fuel.2018.03.047>
- Liu J, Yao K, Xue Y, Zhang XX, Chong ZH, Liang X (2019) Study on fracture behavior of bedded shale in three-point-bending test based on hybrid phase-field modelling. *Theor Appl Fract Mech* 104:102382. <https://doi.org/10.1016/j.tafmec.2019.102382>
- Liu J, Xue Y, Zhang Q, Yao K, Liang X, Wang SH (2020a) Micro-cracking behavior of shale matrix during thermal recovery: Insights from phase-field modeling. *Eng Fract Mech* 239:107301. <https://doi.org/10.1016/j.engfracmech.2020.107301>
- Liu SM, Li XL, Wang DK (2020b) Numerical simulation of the coal temperature field evolution under the liquid nitrogen cold soaking. *Arab J Geosci* 13:1215. <https://doi.org/10.1007/s12517-020-06237-2>
- Liu SM, Li XL, Wang DK, Zhang DM (2021) Experimental study on temperature response of different ranks of coal to liquid nitrogen soaking. *Nat Resour Res* 30:1467–1480. <https://doi.org/10.1007/s11053-020-09768-3>
- Lu YY, Xu ZJ, Li HL, Tang JR, Chen XY (2021) The influences of super-critical CO<sub>2</sub> saturation on tensile characteristics and failure modes of shales. *Energy* 221:119824. <https://doi.org/10.1016/j.energy.2021.119824>
- McDaniel BW, Grundmann SR, Kendrick WD, Wilson DR, Jordan SW (1998) Field applications of cryogenic nitrogen as a hydraulic fracturing fluid. *J Petrol Technol* 50:38–39
- Michot A, Smith DS, Degot S, Gault C (2008) Thermal conductivity and specific heat of kaolinite: evolution with thermal treatment. *J Eur Ceram Soc* 28:2639–2644. <https://doi.org/10.1016/j.jeurceramsoc.2008.04.007>
- Middleton R, Viswanathan H, Currier R, Gupta R (2014) CO<sub>2</sub> as a fracturing fluid: potential for commercial-scale shale gas production and CO<sub>2</sub> sequestration. *Energy Proced* 63:7780–7784. <https://doi.org/10.1016/j.egypro.2014.11.812>
- Nguyen TT, Waldmann D, Bui TQ (2019) Computational chemo-thermo-mechanical coupling phase-field model for complex fracture induced by early-age shrinkage and hydration heat in cement-based materials. *Comput Method Appl M* 348:1–28. <https://doi.org/10.1016/j.cma.2019.01.012>
- Ohtsu M, Okamoto T, Yuyama S (1998) Moment tensor analysis of acoustic emission for cracking mechanisms in concrete. *Acta Struct* 95:87–95
- Pan RK, Cheng YP, Yuan L, Yu MG, Dong J (2014) Effect of bedding structural diversity of coal on permeability evolution and gas disasters control with coal mining. *Nat Hazards* 73:531–546. <https://doi.org/10.1007/s11069-014-1086-7>
- Pelak AJ, Sharma S (2014) Surface water geochemical and isotopic variations in an area of accelerating Marcellus Shale gas development. *Environ Pollut* 195:91–100. <https://doi.org/10.1016/j.envpol.2014.08.016>
- Qin L, Wang P, Li SG, Lin HF, Wang RZ, Wang P, Ma C (2021) Gas adsorption capacity changes in coals of different ranks after liquid nitrogen freezing. *Fuel* 292:120404
- Qin L, Ma C, Li SG, Lin HF, Wang P, Long H, Yan DJ (2022) Mechanical damage mechanism of frozen coal subjected to liquid nitrogen freezing. *Fuel* 309:122124
- Ren S, Fan Z, Zhang L (2013) Mechanisms and experimental study of thermal-shock effect on coal-rock using liquid nitrogen. *Chin J Rock Mech Eng* 32:3790–3794 (in Chinese)
- Sin P, Veinthal R, Sergejev F, Antonov M, Stubna I (2012) Fracture toughness of ceramics fired at different temperatures. *Mater Sci Medzg* 18:90–92. <https://doi.org/10.5755/j01.ms.18.1.1349>
- Su SJ, Gao F, Cai CZ, Du ML, Wang ZK (2020) Experimental study on coal permeability and cracking characteristics under LN<sub>2</sub> freeze-thaw cycles. *J Nat Gas Sci Eng* 83:103526. <https://doi.org/10.1016/j.jngse.2020.103526>
- Su SJ, Hou P, Gao F, Liang X, Ding RY, Cai CZ (2022) Changes in mechanical properties and fracture behaviors of heated marble subjected to liquid nitrogen cooling. *Eng Fract Mech* 261:108256
- Tang SB, Zhang H, Tang CA, Liu HY (2016) Numerical model for the cracking behavior of heterogeneous brittle solids subjected to thermal shock. *Int J Solids Struct* 80:520–531. <https://doi.org/10.1016/j.ijsolstr.2015.10.012>
- Tenner TJ, Lange RA, Downs RT (2007) The albite fusion curve re-examined: new experiments and the high-pressure density and compressibility of high albite and NaAlSi<sub>3</sub>O<sub>8</sub> liquid. *Am Mineral* 92:1573–1585. <https://doi.org/10.2138/am.2007.2464>
- Wang MR, Wang JK, Pan N, Chen SY (2007) Mesoscopic predictions of the effective thermal conductivity for microscale random porous media. *Phys Rev E* 75:036702. <https://doi.org/10.1103/PhysRevE.75.036702>
- Wang YT, Zhou XP, Kou MM (2018) Peridynamic investigation on thermal fracturing behavior of ceramic nuclear fuel pellets under power cycles. *Ceram Int* 44:11512–11542. <https://doi.org/10.1016/j.ceramint.2018.03.214>
- Wang T, Ye X, Liu ZL, Liu XM, Chu DY, Zhuang Z (2020) A phase-field model of thermo-elastic coupled brittle fracture with explicit time integration. *Comput Mech* 65:1305–1321. <https://doi.org/10.1007/s00466-020-01820-6>
- Wu XG, Huang ZW, Li R, Zhang SK, Wen HT, Huang PP, Dai XW, Zhang C (2018) Investigation on the damage of high-temperature shale subjected to liquid nitrogen cooling. *J Nat Gas Sci Eng* 57:284–294. <https://doi.org/10.1016/j.jngse.2018.07.005>
- Wu XG, Huang ZW, Zhang SK, Cheng Z, Li R, Song HY, Wen HT, Huang PP (2019) Damage analysis of high-temperature rocks subjected to LN<sub>2</sub> thermal shock. *Rock Mech Rock Eng* 52:2585–2603. <https://doi.org/10.1007/s00603-018-1711-y>
- Yan H, Tian LP, Feng RM, Mitri H, Chen JZ, He K, Zhang Y, Yang SC, Xu ZJ (2020a) Liquid nitrogen waterless fracking for the environmental protection of arid areas during unconventional resource extraction. *Sci Total Environ* 721:137719. <https://doi.org/10.1016/j.scitotenv.2020.137719>
- Yan H, Tian LP, Feng RM, Mitri H, Chen JZ, Zhang B (2020b) Fracture evolution in coalbed methane reservoirs subjected to liquid nitrogen thermal shocking. *J Cent South Univ* 27:1846–1860. <https://doi.org/10.1007/s11771-020-4412-0>
- Zhai C, Qin L, Liu SM, Xu JZ, Tang ZQ, Wu SL (2016) Pore structure in coal: pore evolution after cryogenic freezing with cyclic liquid nitrogen injection and its implication on coalbed methane extraction. *Energy and Fuel* 30:6009–6020. <https://doi.org/10.1021/acs.energyfuels.6b00920>

**Publisher's Note** Springer Nature remains neutral with regard to jurisdictional claims in published maps and institutional affiliations.